



Numerical investigation of effects of nucleation mechanisms on grain structure in metal additive manufacturing



Xuxiao Li, Wenda Tan*

Department of Mechanical Engineering, The University of Utah, Salt Lake City, Utah 84112, United States

ARTICLE INFO

Keywords:

Metal additive manufacturing
Multi-scale modeling
Nucleation
Solidification
Grain structure

ABSTRACT

Understanding the grain structure in metal additive manufacturing (MAM) builds is important to improve the properties of MAM builds and the controllability of MAM processes. The formation of the columnar and/or equiaxed grains in MAM are caused by an interplay of nucleation and growth mechanisms, which is numerically investigated in this work. A meso-scale Cellular Automata model combined with a macro-scale thermal model is used to predict the three-dimensional grain structure in the direct laser deposition process of stainless steel 304, with the investigation focused on the effects of the nucleation mechanisms (both the epitaxial nucleation at the fusion line and the bulk nucleation in the molten metal) on the grain structure. Our results show that the bulk nucleation condition can significantly change the grain structure (from columnar to equiaxed), and typical grain structures in MAM can be successfully reproduced using different bulk nucleation conditions.

1. Introduction

Metal Additive Manufacturing (MAM) has shown incredible capabilities to manufacture metallic parts with intricate geometries. The geometric flexibility of MAM is owing to the layer-by-layer scanning of a heat source, typically a laser or an electron beam, that melts the metal powder. A bed of metal powder is pre-deposited before the scanning of the heat source, or the metal is fed into the molten pool that is created by the scanning heat source. A wide range of metal alloys are studied in literature, such as iron-based (Stainless Steel 316L [1–3]), aluminum-based (Al-11.28% Si [4], Al-10Si-Mg [5]), titanium-based (Ti-6.5Al-3.5Mo-1.5Zr-0.3Si [6]), and nickel-based (Inconel 718 [7–9]) alloys.

The structural features of the builds by MAM can be categorized as macro-scale $\gtrsim 1000 \mu\text{m}$, e.g., cracks and tears), meso-scale ($\sim 100 \mu\text{m}$, e.g., grain characteristics, lack-of-fusion defects and trapped gas porosity) and micro-scale $\lesssim 10 \mu\text{m}$, e.g., dendrite morphology and phase distribution). The characterization of these structural features is critical to understand MAM processes and helps to construct a map that links process parameters, structural features, and build properties [10]. In this paper, we focus on the meso-scale grain structure.

Despite the variety of MAM processes and metal alloys, certain characteristics of grain structure can be identified from the literature. Both columnar and equiaxed grains are observed in MAM builds. Columnar grains are commonly observed growing epitaxially from the substrate or the previously deposited layer (collectively referred as the

underlying layer) and toward the scanning direction of the heat source [4,8], as shown in Fig. 1. Equiaxed grains can be found distributed among columnar grains. Ref. [9] reported an interesting “sandwich” grain structure where layers of equiaxed grains are observed between every two layers of columnar grains. In general, columnar grains are larger and have a stronger texture than equiaxed grains. Different grain morphology, size, and texture can be achieved by varying the input power, scanning velocity as well as the scanning pattern of the heat source, as widely reported in the literature [1–9].

Theories in welding metallurgy [11] can be conveniently utilized to qualitatively explain the occurrence of the above-mentioned characteristics of grain structure, as both in welding and MAM the metal material is subjected to a moving heat source with high energy input. Upon solidification, nucleation will preferably occur at the fusion line (Fig. 1) due to the lower activation energy. If the layer being built is of the same material as the underlying layer, which is often the case in MAM, the nuclei will preferably adopt the same crystallographic orientations as those of the partially melted grains in the underlying layer. This nucleation mechanism is referred as epitaxial nucleation [11].

After the epitaxial nucleation, grains will grow across the fusion line and along the local temperature gradient direction, which is approximately the local moving direction of the solidification front. This directional solidification leads to columnar grain shapes (the purple grains in Fig. 1). The grains with their certain crystal directions, e.g., the $\langle 1\ 0\ 0 \rangle$ directions for the face-centered-cubic (FCC) and body-centered-cubic (BCC) materials, better aligned with the local temperature

* Corresponding author.

E-mail address: wenda.tan@mech.utah.edu (W. Tan).

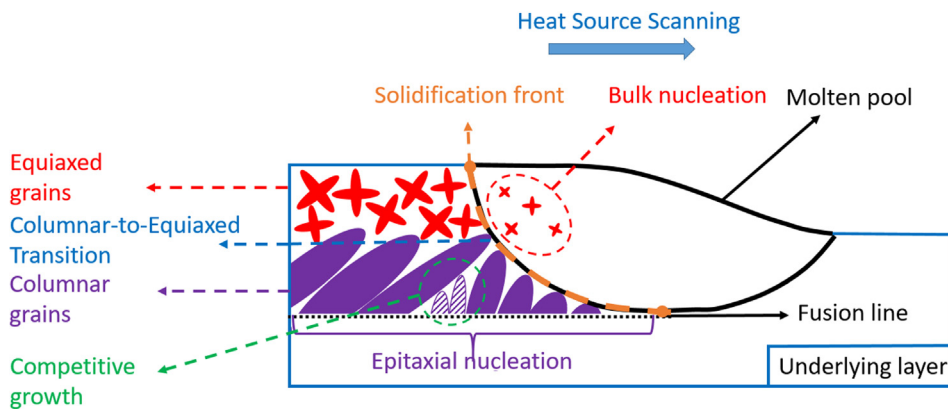


Fig. 1. Summary of possible nucleation and growth mechanisms and their effects on the grain structure in MAM processes.

gradient will outgrow the less aligned ones (such as the shaded purple grains in Fig. 1). This competitive growth mechanism [11] leads to “favored” grains dominating the grain structure, and therefore, larger grains and stronger texture can be observed, as reported in [5,12,13].

Nucleation may also occur in the molten metal ahead of the solidification front, which is referred as the bulk nucleation as opposed to the “surface” epitaxial nucleation at the fusion line (Fig. 1). The nuclei from the bulk nucleation can grow to become equiaxed grains. The equiaxed grains can coexist with columnar grains, or even stop the growth of columnar grains, referred as the Columnar-to-Equiaxed Transition or CET (Fig. 1). In literature, analytical CET models [14–16] have been used to predict the volume percentage of equiaxed grains according to the local thermodynamic conditions of the solidification front. There have been multiple studies that utilize the CET models to explain the grain structure in MAM [7,17,18]. From the above discussion, it can be seen that the grain structure in MAM is complicated by a combination of different mechanisms.

The qualitative welding theories and the analytical CET models, although having a solid physical background, cannot capture the complex scanning patterns in MAM as well as the randomness from a large quantity of grains, and thus fail to quantitatively predict the grain structure in MAM. In light of this, numerical simulations based on physical models have been recently developed to provide quantitative grain structure predictions. In literature, the Cellular Automata (CA) method [13,19–22] and the Monte-Carlo (MC) method [23] have been used to simulate the grain structure in MAM.

Following the seminal work of Rappaz and Gandin [24], several studies have shown the capability of the CA method to capture the major characteristics of the grain structure in MAM. Ref. [13,19] demonstrated the epitaxial nucleation and competitive growth mechanism in their two-dimensional (2D) models; the consequent columnar grain structure and large grain size are successfully reproduced, which are compared with experimental results. Ref. [21] extended the CA method to be three-dimensional (3D); in their multi-pass and multi-layer simulations, a strong texture resulted from the competitive growth was reported. However, these works did not include the bulk nucleation that can cause the occurrence of equiaxed grains. Ref. [20] developed a 2D model which includes the bulk nucleation; in their simulation results, the growth of columnar grains was stopped by equiaxed grains while equiaxed grains could further grow to become “new” columnar grains, which resulted in a laminar grain structure. Ref. [22] developed a similar model but in 3D version. However, only the grain structure of a single pass build is simulated. For the MC method, Ref. [23] qualitatively reproduced the columnar and equiaxed grains observed in experiments, but no detailed discussion is provided regarding the nucleation and growth mechanisms.

Based on the existing literature, it is still not well known the effects of the bulk nucleation on the 3D grain structure, especially in the

complicated cases of multi-layer and/or multi-pass builds. In this work, a 3D CA model is developed that includes both the bulk nucleation and the (surface) epitaxial nucleation, and we will focus on the effects of (both bulk and epitaxial) nucleation mechanisms on the grain structure in MAM. The Direct Laser Deposition (DLD) process and the Stainless Steel (SS) 304 are chosen as a typical MAM process and metal material to demonstrate the model capability. We will describe our modeling methods in Section 2 and modeling results in Section 3. Conclusions and future works will be given in Section 4.

2. Model description

In this work, a macro-scale finite volume model is first implemented to simulate the thermal history in a DLD process. Then a meso-scale CA model is used to simulate the grain structure with the simulated thermal history as a model input.

2.1. Macro-scale thermal history simulation

In this work, we have used the common simplification in MAM modeling that the molten pool flow is ignored [25,26]. A level-set formulation [27] is implemented to implicitly capture the motion of the interface between the metal (solid or liquid) and the gas phase, which is referred as the metal-gas (m-g) interface. The level-set advection equation is written as:

$$\frac{\partial \phi}{\partial t} + F_p |\nabla \phi| = 0, \quad (1)$$

where ϕ is the level-set function. F_p is the interface velocity resulted from the powder deposition in a DLD process, which is determined by a powder flow model described in a previous publication [28]. The level-set function is defined as the signed distance to the m-g interface. As illustrated in Fig. 2, the metal phase has a negative level-set value and the gas phase has a positive level-set value; the zero-level-set iso-contour (the solid blue line) is the location of the m-g interface.

The major physics included in the current model are the heat conduction, the heat convection and radiation at the m-g interface and the thermal energy addition from the laser and the incident powder. The heat conduction equation is written in a conservative form as:

$$\frac{\partial(\rho e)}{\partial t} - \nabla \cdot (k \nabla T) = S, \quad (2)$$

where ρ is the density, e is the internal energy, k is the thermal conductivity, T is the temperature and S is an energy source term. In this work, the material properties, ρ , e , etc., are mixture properties determined by the material properties of different phases. The source term S is distributed over the m-g interface and is composed of several contributions, as given by Eq. (3)

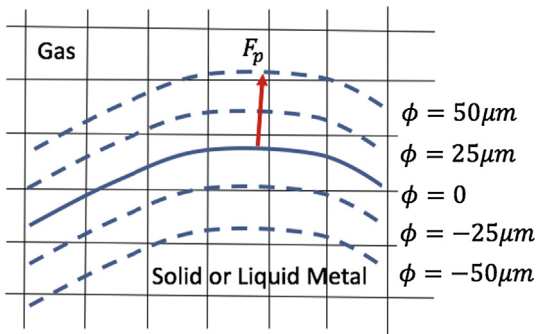


Fig. 2. Illustration of the level-set method. The blue curves are iso-contours of the level-set function ϕ . The solid blue curve is the zero-level-set iso-contour which is the m-g interface; the red arrow indicates the m-g interface velocity F_p . (For interpretation of the references to colour in this figure legend, the reader is referred to the web version of this article.)

$$S = \delta(\phi) \left[\frac{2P\alpha}{\pi r_b^2} \exp\left(-\frac{2r^2}{r_b^2}\right) - h(T-T_0) - \sigma\varepsilon(T^4-T_0^4) + q_p(r) \right], \quad (3)$$

where P is the laser power, α is the laser absorptivity of metal, r is the radial distance from one point to the laser center, r_b is the radius of laser beam, h is the convective heat transfer coefficient, T_0 is the ambient temperature, σ is the Stephan-Boltzmann constant, ε is the metal emissivity, and $\delta(\phi)$ is a smeared delta function given by:

$$\delta(\phi) = \begin{cases} 0 & \text{if } |\phi| > \Delta x \\ \frac{1}{2\Delta x} + \frac{1}{2\Delta x} \cos\left(\frac{\pi\phi}{\Delta x}\right) & \text{if } |\phi| \leq \Delta x \end{cases}, \quad (4)$$

with Δx being the mesh size. The four terms on the right hand side of Eq. (3) represent the heat addition from the scanning laser, the heat loss due to convection, the heat loss due to radiation and the heat addition from powder deposition. We point out that a Gaussian distribution is assumed to represent the heat addition from the scanning laser; in the heat addition term from powder deposition, the function $q_p(r)$ is calculated from a powder flow model. Further explanations of Eqs. (2) and (3) can be found in [28,29].

The computation domain and the Cartesian mesh used for the thermal history simulation are shown in Fig. 3. The laser scans in X-Z plane and the + Y direction is referred as the building direction for a DLD process. The fine mesh (circled by the red¹ dotted line) is a uniform Cartesian mesh with a size of 25 μm . The laser only scans in the fine mesh region to enhance the accuracy of the simulated thermal history. The fine mesh is surrounded by a non-uniform Cartesian coarse mesh which mesh size gradually increases from the fine mesh region outwards. The coarse mesh is used to provide a heat sink to avoid unphysical heat accumulation.

2.2. Meso-scale grain structure simulation

The simulated thermal history $T(x, y, z, t)$ from the macro-scale thermal model is given as an input to the meso-scale grain structure simulations. This thermal history will govern the melting, nucleation, and growth of all grains in the meso-scale model. The meso-scale simulations are conducted on a different Cartesian mesh with a uniform mesh size of 3 μm .

2.2.1. Initialization

At the beginning of the simulation, the computation domain of the meso-scale model should include both substrate and the air regions. In the substrate region, equiaxed grains with different sizes and random

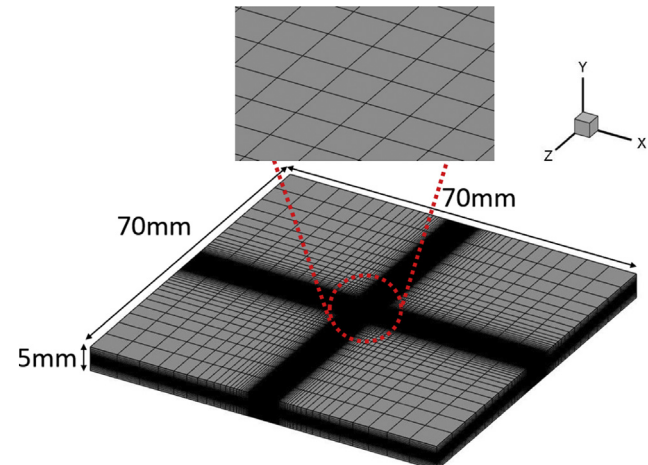


Fig. 3. The Cartesian mesh used for thermal history simulations.

orientations are generated using an original algorithm briefly described as follows. First, cells in the substrate region are randomly selected as the “seed cells”. Each seed is assigned with a random crystal orientation and an imaginary sphere. The imaginary sphere is located at the seed cell centroid with a small initial radius, and it will then grow in size at a slow rate. Once the growing sphere captures a cell in the substrate, the cell will become a part of the grain and is assigned with the crystal orientation as that of the seed for this imaginary sphere. After all the imaginary spheres are fully grown, all cells in the substrate region should be captured by certain sphere and have certain orientation. Cells with the same orientation will form a grain, and each grain covers a certain number of cells in the substrate region. The air region should be adequate in size to cover the built part that will be deposited later. All the cells in the air region will not have an orientation.

As the simulation starts, the molten pool moves with the scanning laser. Some solid cells in the substrate will be covered by the moving molten pool, i.e. the temperature in these cells is above the melting temperature. In this case the solid cells become molten cells, and the orientations of these cells are erased. Some air cells will also be covered by the moving molten pool, indicating that additional molten metal is fed to the local region to replace air. These air cells will also change to molten cells. When the molten pool moves away from these “molten” cells, the local temperature will start to drop, and solidification will take place. The nucleation and grain growth in these cells during the solidification will be simulated with the following algorithms.

2.2.2. Nucleation

Both epitaxial nucleation at the fusion line and the bulk nucleation ahead of the solidification front are numerically captured in the current model.

2.2.2.1. Epitaxial nucleation. we assume immediate nucleation on the fusion line once the local temperature drops below the liquidus temperature. Numerically, when a molten cell is at the fusion line and the temperature drops below the liquidus temperature, a nucleus will be added to this cell. The orientation of this nucleus will be inherited from a neighboring solid cell in the underlying layer.

2.2.2.2. Bulk nucleation. we adopt the empirical approach that the nuclei density N is a continuous function of the local undercooling ΔT (calculated as the difference between the liquidus temperature and the local temperature) [30]. The nuclei density is defined as:

$$N = \int_0^{\Delta T} \frac{dN}{d(\Delta T')} d(\Delta T'), \quad (5)$$

where the distribution $dN/(d(\Delta T))$ describes the increase of nuclei with

¹ For interpretation of color in Figs. 3,5,8, the reader is referred to the web version of this article.

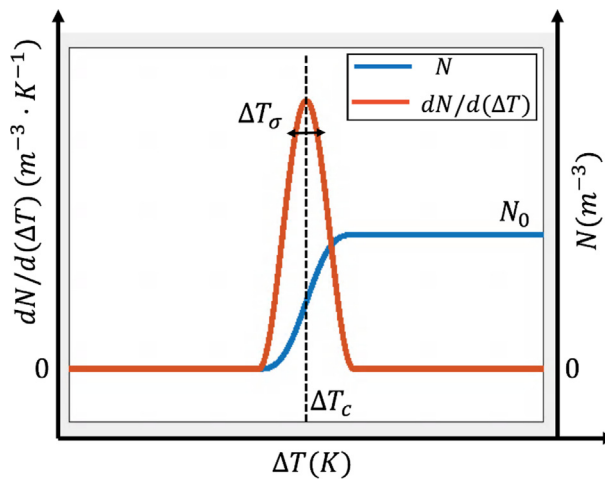


Fig. 4. Illustration of the continuous nucleation approach.

the increase of undercooling. The distribution $dN/(d(\Delta T))$ is assumed to be a Gaussian distribution given by:

$$\frac{dN}{d(\Delta T)} = \frac{N_0}{\Delta T_\sigma \sqrt{2\pi}} \exp\left(-\frac{\Delta T - \Delta T_c}{\sqrt{2}\Delta T_\sigma}\right). \quad (6)$$

N and $dN/(d(\Delta T))$ as functions of ΔT are plotted in Fig. 4. As the undercooling increases to around the critical undercooling ΔT_c , the nuclei density rapidly increases from zero to the maximum nuclei density N_0 .

As can be seen in Fig. 4, a set of nucleation parameters (N_0 , ΔT_c , ΔT_σ) can be used to characterize the bulk nucleation condition. We follow the method in [31] to implement this nucleation mechanism. Before the simulation starts, cells in the computation domain are randomly selected as “nucleation cells” where the nucleation can possibly occur. The number of nucleation cells over the number of all cells will be equal to the maximum nuclei density N_0 . Then, a nucleation undercooling, ΔT_N , is assigned to each nucleation cell. Each nucleation undercooling is generated by a Gaussian probability distribution with ΔT_c as the mean

value and ΔT_σ as the standard deviation. After the simulation starts, if a nucleation cell becomes a molten cell and the undercooling of this nucleation cell is larger than the assigned nucleation undercooling ΔT_N , a nucleus with a random orientation will be added to this nucleation cell.

2.2.3. Growth

Grain growth initiates after the nucleation and is captured by the CA method. In the CA method, the grain preferably grows along certain crystal directions (the $<1\ 0\ 0>$ directions for BCC and FCC materials) and the evolution of the contour of each grain is explicitly tracked by the decentered octahedron growth algorithm [32]. The grain growth velocity is assumed as a function of the local undercooling and is referred as the “growth kinetics”. In a previous publication [33], the authors simulated the grain growth velocity of a single dendrite at different undercooling levels, and used the simulation data to correlate the growth kinetics. In this work, we curve-fit the same simulation data in [33] by a third-order polynomial to obtain the growth kinetics, as given by:

$$V_{\text{grain}}(\Delta T) = a(\Delta T)^3 + b(\Delta T)^2 + c\Delta T + d, \\ a = 1.0909 \times 10^{-5}, \\ b = -2.0336 \times 10^{-4}, \\ c = 2.7397 \times 10^{-3}, \\ d = 1.1504 \times 10^{-4}, \quad (7)$$

where the unit of ΔT is K and the unit of V_{grain} is m/s . The detailed implementation of the CA method for simulating grain structure is well established in the literature [32,34] and will not be discussed here.

3. Result and discussion

In this section, we first briefly discuss the result from the macro-scale thermal history simulation; then we use the same thermal history as the input to the meso-scale grain structure simulation and explore different grain structures under different nucleation conditions. The simulated grain structures will be qualitatively compared with experimental results.

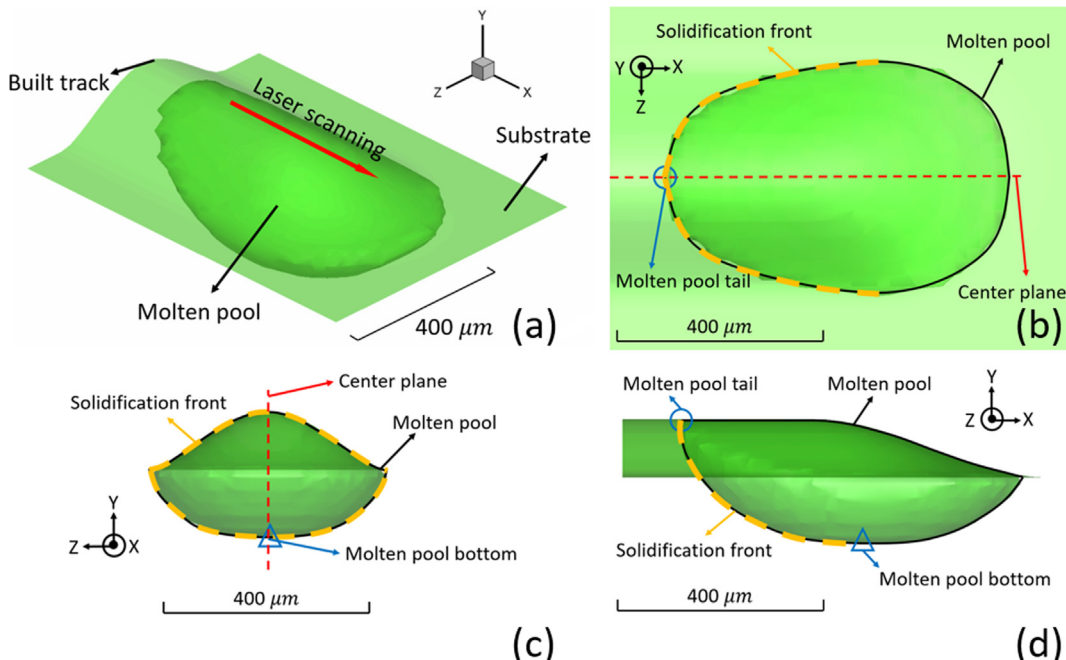


Fig. 5. Thermal history simulation results of a single-pass DLD process. (a): iso-metric view of the built track, the molten pool and the top surface of the substrate. (b)–(d): top view, front view and side view of (a).

Table 1
Material properties of stainless steel 304 and argon.

Property	Stainless steel 304		Argon
	Solid	Liquid	
Density (kg m^{-3})	7200	6900	1.784
Specific heat ($\text{J kg}^{-1} \text{K}^{-1}$)	712	837	520
Thermal conductivity ($\text{W m}^{-1} \text{K}^{-1}$)	19.2	209.2	0.018
Liquidus temperature (K)		1727	
Solidus temperature (K)		1697	
Melting latent heat (J kg^{-1})		274,000	

Table 2
Process parameters of direct laser deposition.

Laser power (W)	200
Scanning velocity (mm s^{-1})	26
Laser beam diameter (μm)	440
Layer increment (μm)	111

3.1. Thermal history

The example simulation results of a single-pass DLD process are shown in Fig. 5. The process parameters and material properties are listed in Tables 1 and 2. Fig. 5a shows the isometric view of the built track, the molten pool and the top surface of the substrate. The laser scans in the $+X$ direction (red arrow). Fig. 5b-d form a three-view diagram of Fig. 5a with molten pool marked by the black solid line. For the convenience of our discussion, the following geometric features of the built track and molten pool are defined. The red dashed line is referred as the center plane with respect to which the built track is symmetric. The blue triangle is referred as the molten pool bottom and the blue circle is referred as the molten pool tail. The orange dashed line marks the solidification front where the liquid metal solidifies.

The simulation of the DLD process can be continued after the first pass. In this work, a “thin-wall” build with 8 layers is simulated, as shown in Fig. 6. The dimensions (X, Y, Z) of the simulated thin-wall build is $1.5 \times 0.89 \times 0.46$ (mm). The laser scans along the $\pm X$ direction (red arrows) and switches scanning direction between every two layers. We will refer for the rest of the paper the $+X$ direction as the scanning direction (SD), the $+Y$ direction as the building direction (BD), the $+Z$ direction as the transverse direction, the planes parallel to the X-Y plane as the longitudinal sections, and the planes parallel to the Y-Z plane as the cross-sections.

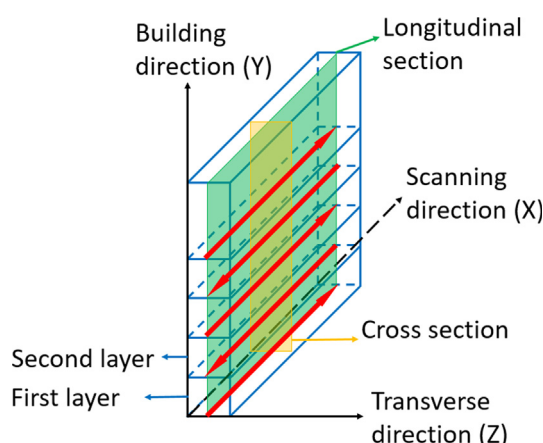


Fig. 6. The laser scanning strategy for the thin-wall simulation.

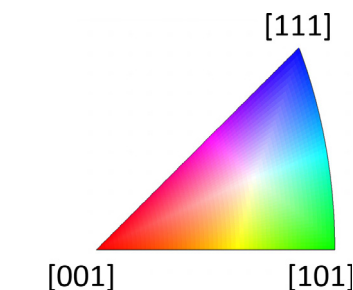


Fig. 7. The IPFOM color key.

3.2. Grain structure of single-pass build

We first study the grain structure of a single-pass with the thermal history in Fig. 5 to identify key features of the grain structure in MAM. The grain structure is examined at typical longitudinal sections and cross-sections. In this work, the grain orientations are presented by the Inverse Pole Figure Orientation Mapping (referred as IPFOM). The IPFOMs presented in this work are defined with respect to the building direction, unless otherwise specified. When necessary, we also calculate the Orientation Distribution Function (ODF) from the IPFOM and plot the (1 0 0) Pole Figure (referred as PF) of the ODF. The IPFOMs and PFs are all generated using the Matlab toolbox MTEX. The color key of the IPFOMs throughout this work is shown in Fig. 7. We will first discuss a simulation without any bulk nucleation (by setting the N_0 to be zero) to verify the epitaxial nucleation and competitive growth mechanism captured by the CA method; then the more complicated cases with the bulk nucleation will be discussed.

3.2.1. Without bulk nucleation

The grain structure examined at the center plane of the built track and a cross section during the building process are shown in Fig. 8a and b. The fusion line (black dotted line) is defined as the partition line between un-melted and melted metal when examining a 2D section. As can be seen in Fig. 8a and b, the epitaxial nucleation initiates at the fusion line and the grains grow across the fusion line. In Fig. 8a, it is observed that the columnar grains dominate the grain structure and tend to grow perpendicular to the moving solidification front (orange dashed line). At the cross-section, although many grains seem to be equiaxed, they are actually the columnar grains growing into the cross-section plane. The competitive growth mechanism can be observed in Fig. 8a; some grains (e.g., grain B) are outgrown by more “favored” grains (e.g., grain A) whose $\langle 1 0 0 \rangle$ directions are better aligned with the local temperature gradient direction (the local moving direction of the solidification front). To demonstrate this, the (1 0 0) PF calculated from the IPFOM in Fig. 8a is plotted in Fig. 8c along with the individual orientations of grain A and B. A fiber texture is observed in Fig. 8c where the grains have one of their $\langle 1 0 0 \rangle$ axes aligned with the white dashed line (referred as the fiber) in the BD-SD plane, while the other two $\langle 1 0 0 \rangle$ axes are free, forming a band across the pole figure. Similar fiber texture is also reported by the experimental work of [35]. The fiber texture is due to the competitive growth which results in the preference of the $\langle 1 0 0 \rangle$ directions towards the local moving direction of the solidification front. It can be observed in Fig. 8c that a typical dominating grain (grain A) has its orientation aligned with the fiber, while a typical grain being outgrown (grain B) has its orientation deviating from the fiber.

3.2.2. With bulk nucleation

The effects of bulk nucleation parameters (Fig. 4), N_0 and ΔT_c , on the grain structure are investigated; ΔT_c is fixed as a small number in the following discussion because we find its effects on the grain structure are relatively insignificant. Before the discussion of the effects of bulk nucleation, we use Hunt’s CET model [15] to predict the grain

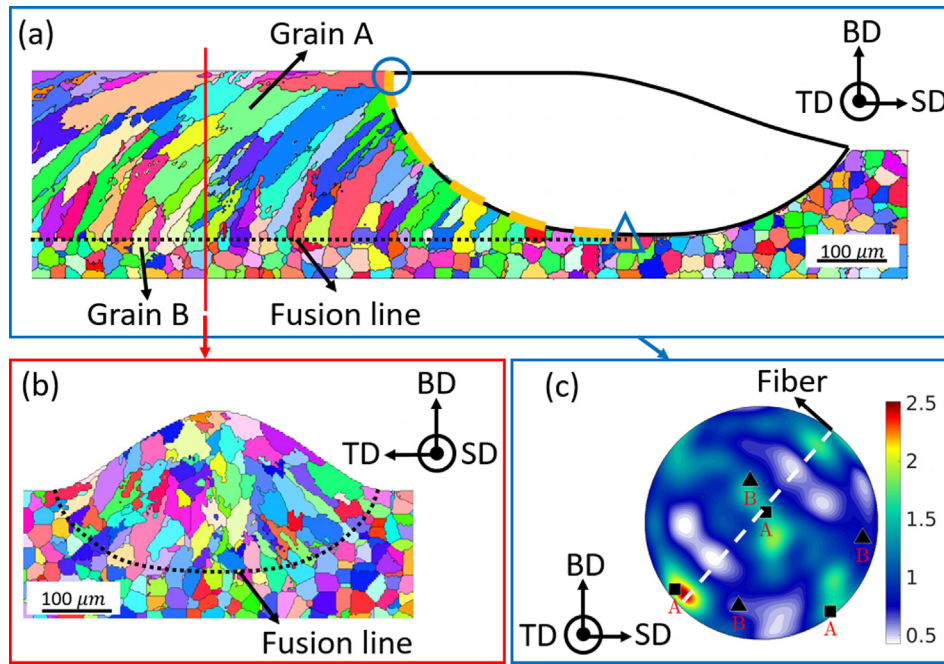


Fig. 8. Single-pass grain structure during the building process without bulk nucleation. (a) and (b): the IPFOMs with respect to the building direction; (a): center plane and (b): cross-section. (c): the (1 0 0) PF calculated from (a).

morphology according to the “G-V condition” of the simulated thermal history. The prediction from Hunt’s CET model will be used to verify the simulated grain structure with the bulk nucleation.

The G-V condition is characterized by the temperature gradient G on and the velocity V of the solidification front [17], which are calculated as:

$$G = \sqrt{\left(\frac{\partial T}{\partial x}\right)^2 + \left(\frac{\partial T}{\partial y}\right)^2 + \left(\frac{\partial T}{\partial z}\right)^2} \quad (8a)$$

$$V = V_{laser} \cos\theta \quad (8b)$$

$$\cos\theta = \frac{\partial T / \partial x}{G} \quad (8c)$$

where V_{laser} is the scanning velocity of laser. To find the grain structure prediction with Hunt’s CET model, we evenly sample points on the solidification front and plot the (G, V) of the sampled points as a scatter plot in Fig. 9. The scatter plot is colorized according to the vertical distance between a sampled point to the molten pool bottom, $y - y_b$, with y_b being the y coordinate of the molten pool bottom. The (G, V) of the molten pool bottom and tail are marked out by the blue triangle and circle. The orange polygon marks the region covered by the scatter plot. We then use Hunt’s CET model to calculate the demarcation curves between different categories of grain structures (columnar, equiaxed, and mixed), plotted as the red curves in Fig. 9.

It is observed in the Fig. 9 that as the G decreases and the V increases, the grain structure will transit from columnar to equiaxed. It can be also seen that the scattered dots with a relatively small $y - y_b$ (e.g., the molten pool bottom where $y - y_b = 0$) sit at the lower right part of the G-V map (columnar region); the scattered dots with a relatively large $y - y_b$ (e.g., the molten pool tail where $y - y_b = 234 \mu m$) sit at the upper left part of the G-V map (equiaxed region). Therefore, it is expected from Hunt’s model that the grains will be increasingly equiaxed along the building direction.

We now study the effects of N_0 and ΔT_c on the single-pass grain structure using the $(N_0, \Delta T_c)$ listed in Table 3. Case 1–3 are used to study the effects of N_0 on the grain structure with ΔT_c fixed as 5 K and N_0 varied as $5 \times 10^{13} m^{-3}$, $5 \times 10^{14} m^{-3}$, and $5 \times 10^{15} m^{-3}$. Case 2, 4 and 5 are used to study the effects of ΔT_c on the grain structure with N_0

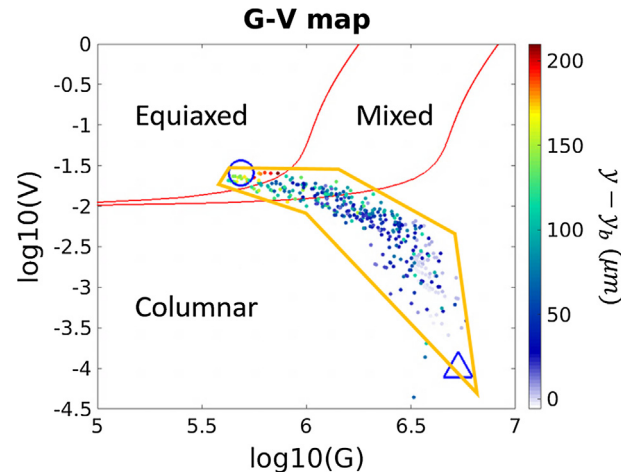


Fig. 9. The G-V map. The red curves are calculated using Hunt’s model with N_0 being $10^{14} m^{-3}$ and ΔT_c being 5 K. The scatter plot is calculated from the simulated thermal history. (For interpretation of the references to colour in this figure legend, the reader is referred to the web version of this article.)

Table 3
Nucleation parameters in single-pass simulations.

Case	$N_0 (m^{-3})$	$\Delta T_c (K)$
1	5×10^{13}	5
2	5×10^{14}	5
3	5×10^{15}	5
4	5×10^{14}	0
5	5×10^{14}	10

fixed as $5 \times 10^{14} m^{-3}$ and ΔT_c varied as 0 K, 5 K, and 10 K.

The simulated grain structures at the center plane of the built track for Case 1–3 are shown in Fig. 10a–c. The corresponding G-V map, calculated with Hunt’s CET model as in Fig. 9, is given in Fig. 10d. The (G, V) of the solidification front is indicated by the orange polygon as in Fig. 9. Due to the epitaxial nucleation, the grains still grow across the

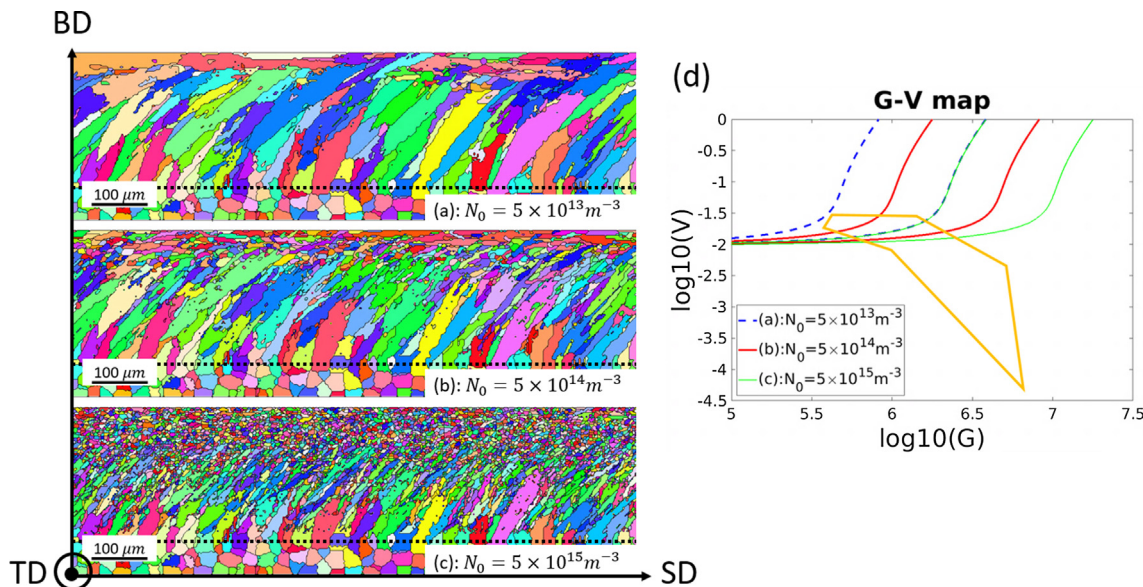


Fig. 10. The effects of N_0 on grain structure. ΔT_c is kept as 5 K. (a)–(c): the grain structures at the center plane with N_0 being $10^{13} m^{-3}$, $10^{14} m^{-3}$, and $10^{15} m^{-3}$. The IPFOMs are plotted with respect to the building direction. (d): the G-V map obtained with different values of N_0 .

fusion line (the black dotted line) to form columnar grains; but when the bulk nucleation is included, equiaxed grains can also be seen dispersed among columnar grains. From Fig. 10a–c it is observed that the number of equiaxed grains is increased as N_0 increases; this trend can be reflected in Fig. 10d where the orange polygon does not overlap with the equiaxed region when N_0 is the smallest ($5 \times 10^{13} m^{-3}$), while a significant portion of the orange polygon is within the equiaxed region when N_0 is the largest ($5 \times 10^{15} m^{-3}$). It can be observed in Fig. 10b and c that the grains are columnar near the fusion line, and the grains generally become increasingly dominated by equiaxed grains along the building direction. In Fig. 10c, a CET is observed where the nuclei density is large enough such that the growth of columnar grains is blocked by the equiaxed grains resulted from the bulk nucleation. This change of grain morphology along the building direction agrees with the prediction from Hunt's CET model as explained in Fig. 9.

Next, the simulated grain structures at the center plane of the built

track for Case 2, 4 and 5 (Table 3) are shown in Fig. 11a–c and the corresponding G-V map is shown in Fig. 11d. From Fig. 11a–c it is observed that the number of equiaxed grains decreases as ΔT_c increases, which is verified in Fig. 11d where a significant portion of the orange polygon is within the mixed and equiaxed region when ΔT_c is the smallest (0 K), while the orange polygon is almost entirely within the columnar region when ΔT_c is the largest (10 K). This observation can be caused by that the critical undercooling ΔT_c acts as a nucleation barrier. Higher ΔT_c means that a higher undercooling is required, and therefore, less likelihood there is for the bulk nucleation to occur.

3.3. Grain structure of thin-wall build

The grain structures of an 8-layer thin-wall build are simulated using three different sets of nucleation parameters (N_0 , ΔT_c) as listed in Table 4. The nucleation parameters are chosen such that the bulk

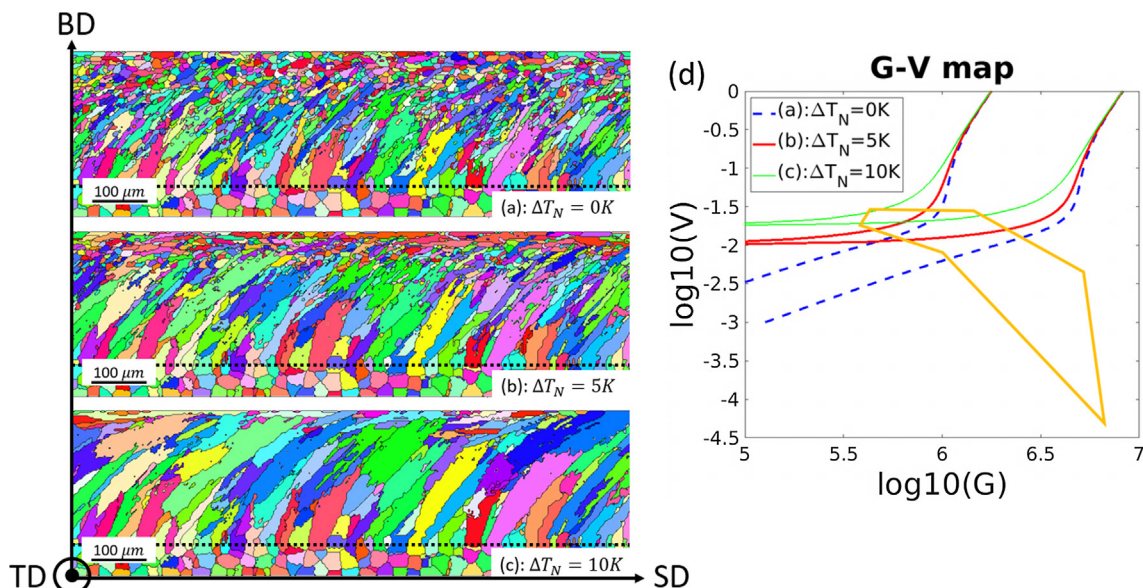


Fig. 11. The effects of ΔT_c on grain structure. N_0 is kept as $5 \times 10^{14} m^{-3}$. (a)–(c): the grain structures at the center plane with ΔT_c being 0 K, 5 K, and 10 K. The IPFOMs are plotted with respect to the building direction. (d): The G-V map obtained with different values of ΔT_c .

Table 4
Nucleation parameters in thin-wall simulations.

Case	N_0 (m^{-3})	ΔT_c (K)
6	5×10^{13}	10
7	5×10^{14}	0
8	2×10^{15}	0

nucleation is increasingly encouraged from Case 6–8 in Table 4. Case 6 represents the case where nearly no bulk nucleation occurs and Case 8 includes enough bulk nucleation so that a CET will occur. The simulation results of Case 6–8 are qualitatively compared with experimental thin-wall builds [4,8,9], as presented in Figs. 12–14. It should be noted that the experimental builds are for different metal alloys and have different dimensions than the simulation builds, but the scanning strategy of the experimental builds is the same as that in Fig. 6. For each case, the grain structure on a typical longitudinal section (not necessarily the center plane) is examined to compare with the experimental result. We also compare for each case the IPFOM color key as well as the (1 0 0) PF calculated from the IPFOM between simulation and experimental results. To extract more quantitative information from simulated grain structures, the 2D grain size and aspect ratio

distribution from the selected longitudinal sections are calculated using the Matlab toolbox MTEX, as shown in Fig. 15. When calculating the grain quantitative information and the PFs, we use a longitudinal section of the dimensions (X, Y) of 1.5×0.89 mm, which is large enough compared with the typical grain size to avoid any significant statistical bias. We point out that the longitudinal sections are only partially shown for the IPFOMs in Figs. 12d, 13d and 14d.

It is observed from Figs. 12–14 that in both simulation and experimental results, the grain growth follows the zig-zag scanning pattern of laser, leading to tortuous grain shapes. The nucleation parameters from Case 6 to 8 lead to more equiaxed and smaller grains, which is supported by the decreasing grain aspect ratio and the decreasing grain size from Case 6 to 8 in Fig. 15. Interestingly, the (1 0 0) PFs from simulations (Figs. 12f, 13f and 14f) exhibit the similar cube texture as that from experimental PFs (Figs. 12c, 13c and 14c). As analyzed in [4], the zig-zag scanning pattern of laser creates two preferred directions for the $\langle 1 0 0 \rangle$ directions of grains. Therefore, two and equivalently all three axes of the $\langle 1 0 0 \rangle$ directions are “fixed” and consequently a cube texture can be developed. The current model has shown the capability to predict this texture development. It is also noted that the cube texture becomes weaker from Case 6 to 8. The texture index calculated from Figs. 12f, 13f and 14f, is 3.98, 2.40 and 1.44. This can be attributed to the increasing amount of nucleation

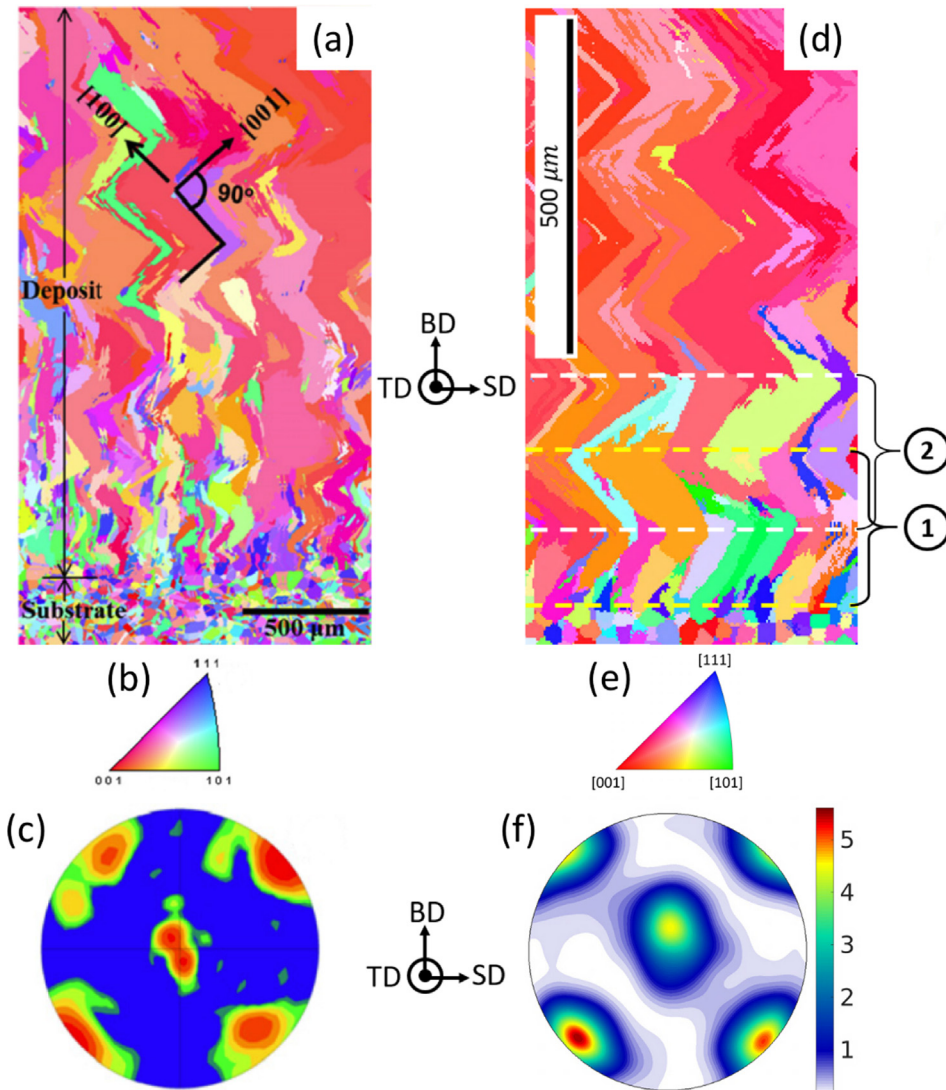


Fig. 12. Comparison between simulation and experimental results for Case 6 ($N_0 = 5 \times 10^{13} \text{ m}^{-3}$, $\Delta T_N = 10 \text{ K}$). (a)–(c): experimental results from [8]. (d)–(f): simulation results. (a) and (b): the IPFOM with respect to the transverse direction. (c) and (d): the IPFOM color key. (e) and (f): the (1 0 0) PF calculated from IPFOM.

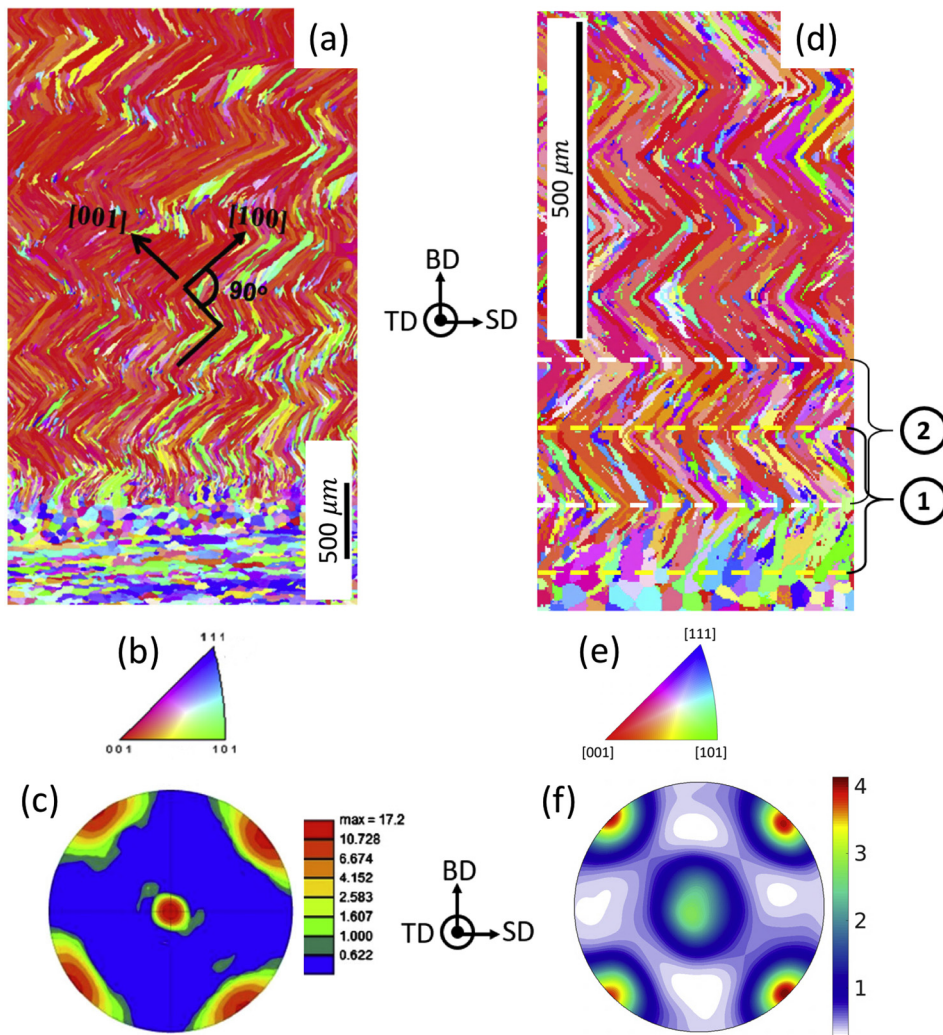


Fig. 13. Comparison between simulation and experimental results for Case 7 ($N_0 = 5 \times 10^{14} \text{ m}^{-3}$, $\Delta T_N = 0 \text{ K}$). (a)–(c): experimental results from [4]. (d)–(f): simulation results. (a) and (b): the IPFOM with respect to the transverse direction. (c) and (d): the IPFOM color key. (e) and (f): the (1 0 0) PF calculated from IPFOM.

which introduces more random orientations and thus weakens the texture. The simulated grain structures can be better understood by examining the grain structure from the first two layers, as marked by the yellow and white dashed lines in Figs. 12d, 13d and 14d.

- In Fig. 12d, since the bulk nucleation is rare, the first layer is dominated by the columnar grain. For the same reason, the existing grains from the first layer can continue to grow in the second layer and compete with each other along the building direction. As the building process continues, several very coarse grains finally survive and dominate the grain structure, which can be compared to the experimentally observed grain structure in Fig. 12a.
- In Fig. 13d, new grains are introduced by the bulk nucleation; the first layer is mixed with both columnar and equiaxed grains. When the second layer is built, part of the first layer is remelted, and the partially remelted equiaxed grains from the first layer can grow to become columnar grains in the second layer and join the competitive growth. Since new “competitors” can be constantly introduced, chances are reduced that several grains can outgrow all the other grains. Therefore, no significant grain coarsening is found in Fig. 13d; instead, tortuous, needle-like grains are observed, which can be compared to the experimentally observed grain structure in Fig. 13a.
- For Fig. 14d, as more bulk nucleation is introduced, a CET occurs in the first layer such that a layer of equiaxed grains form at the very

top of the first layer (similar to the result in Fig. 10c). When the second layer is built, only part of the “equiaxed layer” is remelted; the partially remelted equiaxed grains can become columnar grains in the second layer; the un-remelted equiaxed grains in the first layer will stay as they are. As this pattern repeats in the building direction, layers of equiaxed grains can be found sandwiched between every two layers of columnar grains, which can be compared to the experimentally observed grain structure in Fig. 14a.

4. Conclusion

In this work, a 3D CA model is implemented to simulate the meso-scale grain structure in MAM processes. The bulk nucleation is considered in our model and is characterized by two nucleation parameters, the maximum nuclei density N_0 and the critical undercooling ΔT_c . The meso-scale grain structure simulation is carried out using the input from the macro-scale thermal history simulation.

The major findings from the current work can be summarized as follows:

- The current model demonstrates the capability of capturing the mechanisms of the epitaxial nucleation, the competitive growth, the bulk nucleation, and the CET in MAM. The simulated grain structures from the current model are qualitatively verified by both experimental results and analytical models.

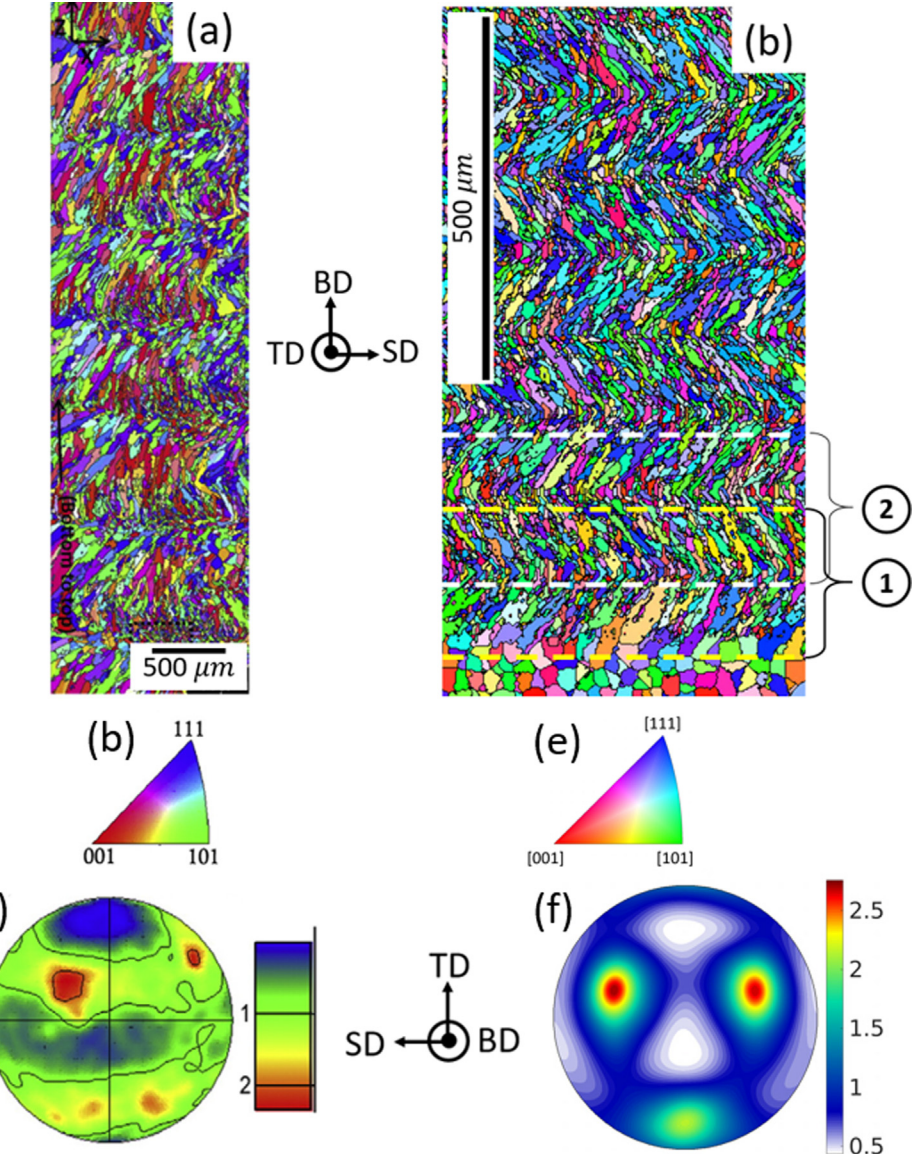


Fig. 14. Comparison between simulation and experimental results for Case 8 ($N_0 = 2 \times 10^{15} \text{ m}^{-3}$, $\Delta T_N = 0 \text{ K}$). (a)–(c): experimental results from [9]. (d)–(f): simulation results. (a) and (b): the IPFOM with respect to the building direction. (c) and (d): the IPFOM color key. (e) and (f): the (1 0 0) PF calculated from IPFOM. Notice that the projection direction of the PF in (f) are adjusted to match with (c).

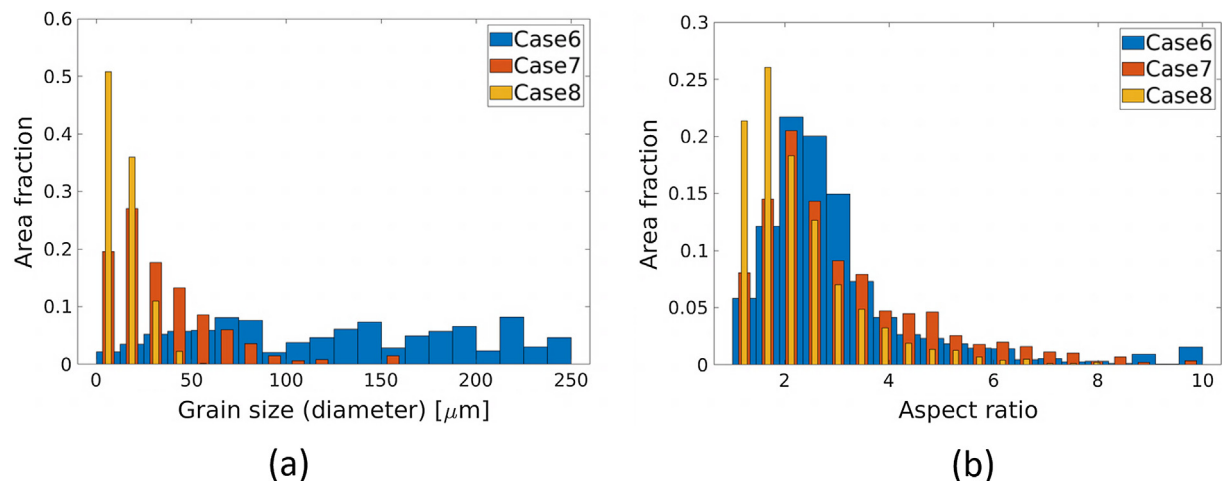


Fig. 15. Quantitative grain structure information from Case 6–8. (a): grain size distribution. (b): grain aspect ratio distribution.

- It is found that the nucleation parameters (N_0 , ΔT_c) can significantly affect the grain structure. An increase of N_0 and/or a decrease of ΔT_c will encourage the occurrence of equiaxed grains, while a decrease of N_0 and/or an increase of ΔT_c will make the grain structure more dominated by columnar grains.
- There is a wide range of possible nucleation parameters for real MAM processes; using different nucleation parameters we can replicate three very different grain structures in MAM, all of which have been found experimentally.

There are several limitations of the current work and we list the following tasks as future works:

- There is a lack of quantitative validation of the simulated grain structure. Experiments need to be conducted to first calibrate the unknown nucleation parameter (N_0 , ΔT_c) after which the simulated grain structure can be quantitatively compared with experiments.
- There are other potential nucleation mechanisms that need to be included in the current model. For example, it has been found but not well understood that new grains can form at the fusion line with different orientations than the underlying layer [5]. It is possible that non-epitaxial nucleation [11] needs to be considered to capture this phenomenon.
- The thin-wall build is used in this work to demonstrate the model capability. More complicated build geometry and scanning strategy will be studied in the future.

Acknowledgment

The authors wish to gratefully acknowledge the financial support provided for this study by the startup funds from the University of Utah and the technical support from the Center for High-Performance Computing at the University of Utah.

References

- T. Niendorf, S. Leuders, A. Riemer, H.A. Richard, T. Tröster, D. Schwarze, Highly anisotropic steel processed by selective laser melting, *Metall. Mater. Trans. B* 44 (2013) 794–796.
- T. Niendorf, S. Leuders, A. Riemer, F. Brenne, T. Tröster, H.A. Richard, D. Schwarze, Functionally graded alloys obtained by additive manufacturing, *Adv. Eng. Mater.* 16 (2014) 857–861.
- T.T. Roehling, S.S. Wu, S.A. Khairallah, J.D. Roehling, S.S. Soezeri, M.F. Crumb, M.J. Matthews, Modulating laser intensity profile ellipticity for microstructural control during metal additive manufacturing, *Acta Mater.* 128 (2017) 197–206.
- G. Dinda, A. Dasgupta, J. Mazumder, Evolution of microstructure in laser deposited Al-11.28% Si alloy, *Surf. Coat. Technol.* 206 (2012) 2152–2160.
- L. Thijss, K. Kempen, J.-P. Kruth, J. Van Humbeeck, Fine-structured aluminium products with controllable texture by selective laser melting of pre-alloyed AlSi10Mg powder, *Acta Mater.* 61 (2013) 1809–1819.
- T. Wang, Y. Zhu, S. Zhang, H. Tang, H. Wang, Grain morphology evolution behavior of titanium alloy components during laser melting deposition additive manufacturing, *J. Alloy. Compd.* 632 (2015) 505–513.
- H. Helmer, A. Bauereiß, R. Singer, C. Körner, Grain structure evolution in Inconel 718 during selective electron beam melting, *Mater. Sci. Eng., A* 668 (2016) 180–187.
- G. Dinda, A. Dasgupta, J. Mazumder, Texture control during laser deposition of nickel-based superalloy, *Scr. Mater.* 67 (2012) 503–506.
- L.L. Parimi, G. Ravi, D. Clark, M.M. Attallah, Microstructural and texture development in direct laser fabricated IN718, *Mater. Charact.* 89 (2014) 102–111.
- T. DebRoy, H. Wei, J. Zuback, T. Mukherjee, J. Elmer, J. Milewski, A. Beese, A. Wilson-Heid, A. De, W. Zhang, Additive manufacturing of metallic components—process, structure and properties, *Prog. Mater Sci.* (2017).
- S. Kou, *Welding Metallurgy*, John Wiley & Sons, 2003.
- L. Thijss, M.L.M. Sistiaga, R. Wauthle, Q. Xie, J.-P. Kruth, J. Van Humbeeck, Strong morphological and crystallographic texture and resulting yield strength anisotropy in selective laser melted tantalum, *Acta Mater.* 61 (2013) 4657–4668.
- J. Zhang, F. Liou, W. Seufzer, K. Taminger, A coupled finite element cellular automaton model to predict thermal history and grain morphology of Ti-6Al-4V during direct metal deposition (DMD), *Addit. Manuf.* 11 (2016) 32–39.
- M. Gäumann, R. Trivedi, W. Kurz, Nucleation ahead of the advancing interface in directional solidification, *Mater. Sci. Eng., A* 226 (1997) 763–769.
- J. Hunt, Steady state columnar and equiaxed growth of dendrites and eutectic, *Mater. Sci. Eng.* 65 (1984) 75–83.
- W. Kurz, C. Bezençon, M. Gäumann, Columnar to equiaxed transition in solidification processing, *Sci. Technol. Adv. Mater.* 2 (2001) 185–191.
- Z. Liu, H. Qi, Effects of substrate crystallographic orientations on crystal growth and microstructure formation in laser powder deposition of nickel-based superalloy, *Acta Mater.* 87 (2015) 248–258.
- N. Raghavan, R. Dehoff, S. Pannala, S. Simunovic, M. Kirka, J. Turner, N. Carlson, S.S. Babu, Numerical modeling of heat-transfer and the influence of process parameters on tailoring the grain morphology of IN718 in electron beam additive manufacturing, *Acta Mater.* 112 (2016) 303–314.
- A. Rai, H. Helmer, C. Körner, Simulation of grain structure evolution during powder bed based additive manufacturing, *Addit. Manuf.* 13 (2017) 124–134.
- O. Lopez-Botello, U. Martinez-Hernandez, J. Ramírez, C. Pinna, K. Mumtaz, Two-dimensional simulation of grain structure growth within selective laser melted AA-2024, *Mater. Des.* 113 (2017) 369–376.
- O. Zinovieva, A. Zinoviev, V. Ploshikhin, Three-dimensional modeling of the microstructure evolution during metal additive manufacturing, *Comput. Mater. Sci.* 141 (2018) 207–220.
- C. Panwisawas, C. Qiu, M.J. Anderson, Y. Sovani, R.P. Turner, M.M. Attallah, J.W. Brooks, H.C. Basalto, Mesoscale modelling of selective laser melting: thermal fluid dynamics and microstructural evolution, *Comput. Mater. Sci.* 126 (2017) 479–490.
- T.M. Rodgers, J.D. Madison, V. Tikare, Simulation of metal additive manufacturing microstructures using kinetic Monte Carlo, *Comput. Mater. Sci.* 135 (2017) 78–89.
- A. Kaplan, Laser absorptivity on wavy molten metal surfaces: categorization of different metals and wavelengths, *J. Laser Appl.* 26 (2014) 012007.
- W. King, A. Anderson, R. Ferencz, N. Hodge, C. Kamath, S. Khairallah, A. Rubenchik, Laser powder bed fusion additive manufacturing of metals: physics, computational, and materials challenges, *Appl. Phys. Rev.* 2 (2015) 041304.
- M. Markl, C. Körner, Multi-scale modeling of powder-bed-based additive manufacturing, *Annu. Rev. Mater. Res.* 46 (2016) 1–34.
- S.O.R. Fedkiw, S. Osher, Level set methods and dynamic implicit surfaces, *Surfaces* 44 (2002) 77.
- S. Wen, Y.C. Shin, Modeling of transport phenomena during the coaxial laser direct deposition process, *J. Appl. Phys.* 108 (2010) 044908.
- H. Qi, J. Mazumder, H. Ki, Numerical simulation of heat transfer and fluid flow in coaxial laser cladding process for direct metal deposition, *J. Appl. Phys.* 100 (2006) 024903.
- M. Rappaz, C.-A. Gandin, Probabilistic modelling of microstructure formation in solidification processes, *Acta Metall. et Materialia* 41 (1993) 345–360.
- M. Rappaz, C.A. Gandin, J.-L. Desbiolles, P. Thevoz, Prediction of grain structures in various solidification processes, *Metall. Mater. Trans. A* 27 (1996) 695–705.
- C.-A. Gandin, J.-L. Desbiolles, M. Rappaz, P. Thevoz, A three-dimensional cellular automation-finite element model for the prediction of solidification grain structures, *Metall. Mater. Trans. A* 30 (1999) 3153–3165.
- W. Tan, Y.C. Shin, Multi-scale modeling of solidification and microstructure development in laser keyhole welding process for austenitic stainless steel, *Comput. Mater. Sci.* 98 (2015) 446–458.
- C.-A. Gandin, M. Rappaz, A 3D cellular automaton algorithm for the prediction of dendritic grain growth, *Acta Mater.* 45 (1997) 2187–2195.
- V. Ocelík, I. Furár, J.T.M. De Hosson, Microstructure and properties of laser clad coatings studied by orientation imaging microscopy, *Acta Mater.* 58 (2010) 6763–6772.